

Entangled Nanoplasmonic Cavities for Estimating Thickness of Surface-Adsorbed Layers

Amideddin Mataji-Kojouri, Mehmet Ozgun Ozen, Mahmoud Shahabadi,* Fatih Inci,* and Utkan Demirci*



Cite This: <https://dx.doi.org/10.1021/acsnano.0c02797>



Read Online

ACCESS |



Metrics & More



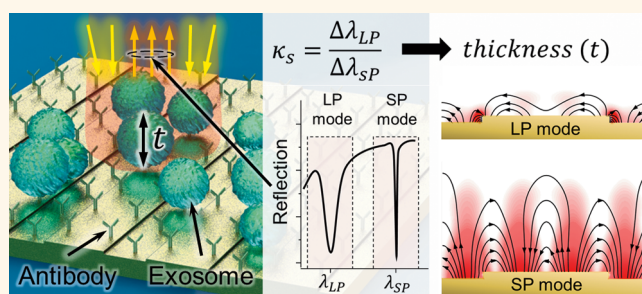
Article Recommendations



Supporting Information

ABSTRACT: Plasmonic sensors provide real-time and label-free detection of biotargets with unprecedented sensitivity and detection limit. However, they usually lack the ability to estimate the thickness of the target layer formed on top of the sensing surface. Here, we report a sensing modality based on reflection spectroscopy of a nanoplasmonic Fabry–Perot cavity array, which exhibits characteristics of both surface plasmon polaritons and localized plasmon resonances and outperforms its conventional counterparts by providing the thickness of the surface-adsorbed layers. Through numerical simulations, we demonstrate that the designed plasmonic surface resembles two entangled Fabry–Perot cavities excited from both ends. Performance of the device is evaluated by studying sensor response in the refractive index (RI) measurement of aqueous glycerol solutions and during formation of a surface-adsorbed layer consisting of protein (*i.e.*, NeutrAvidin) molecules. By tracking the resonance wavelengths of the two modes of the nanoplasmonic surface, it is therefore possible to measure the thickness of a homogeneous adsorbed layer and RI of the background solution with precisions better than 4 nm and 0.0001 RI units. Using numerical simulations, we show that the thickness estimation algorithm can be extended for layers consisting of nanometric analytes adsorbed on an antibody-coated sensor surface. Furthermore, performance of the device has been evaluated to detect exosomes. By providing a thickness estimation for adsorbed layers and differentiating binding events from background RI variations, this device can potentially supersede conventional plasmonic sensors.

KEYWORDS: plasmonic biosensors, microfluidics, point-of-care devices, plasmonic sizing, Fabry–Perot resonator, surface plasmon resonance



By offering rapid and label-free detection, plasmonics is a promising solution in many research fields and applications, especially for diagnosis and screening technologies as well as environmental monitoring and quality control.^{1–8} Conventional plasmonic approaches are designed to capture and detect biotargets on antibody-coated sensor surfaces. These sensors cannot usually distinguish whether the detected binding event is due to adsorption of a thin layer of high refractive index (RI) or a thicker layer with lower RI. Estimating thickness of a biotarget layer formed on the sensor is beneficial in various applications. For example, functionality of exosomes which are involved in different neurodegenerative and cardiovascular disorders and cancers^{9–14} is highly size-dependent. The size of exosomes is a determinant factor in their possible uptake by cells and their efficiency in drug delivery.¹⁵ Recently, it was found that oral cancer will present increased size and intervesicular aggregation of saliva

exosomes.¹⁶ The same phenomenon is observed in urinary exosomes of patients with prostate cancer.¹⁷ Hence, realization of a plasmonic sensor which provides size estimation would be of clinical interest especially in early cancer detection. In this regard, a dual-wavelength prism-based plasmonic sensor was suggested recently for sizing of biological nanoparticles.¹⁸ However, large propagation lengths of the excited surface plasmons decrease its lateral resolution, and the system is based on a complex measurement setup and requires highly

Received: April 2, 2020

Accepted: May 13, 2020

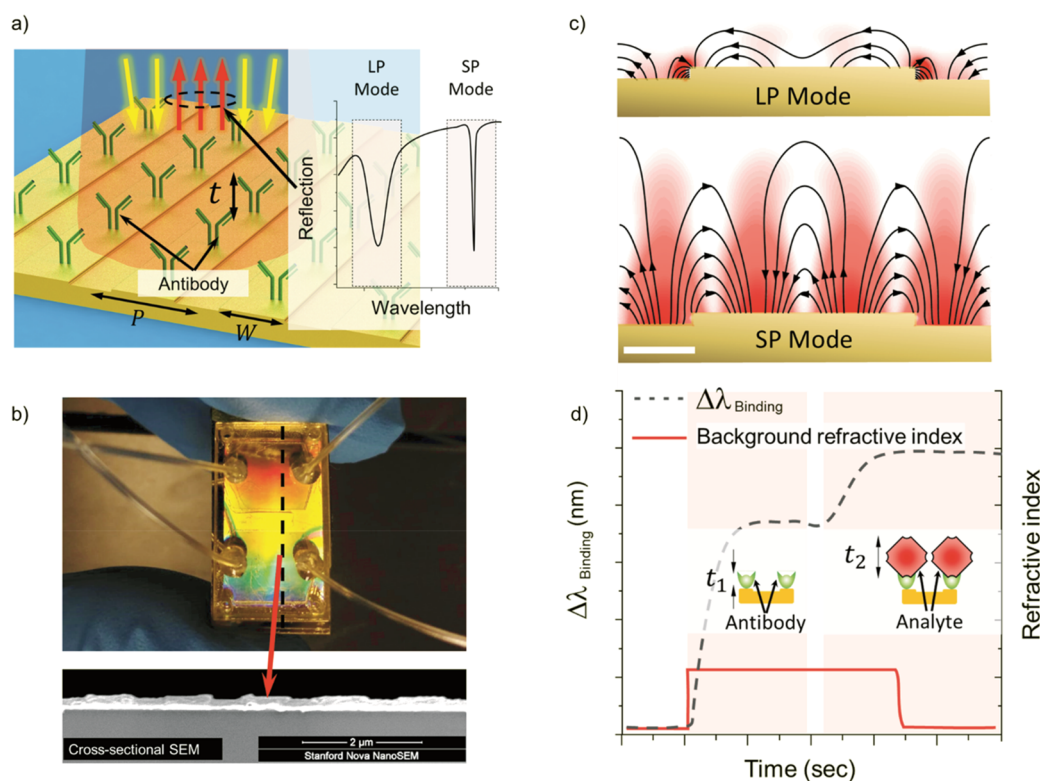


Figure 1. Detection and characterization with plasmonic Fabry–Perot cavities. (a) Illustration of the periodic nanoplasmonic surface covered with antibodies for detection of cellular entities and a typical reflection spectrum from the structure. Periodicity of the nanostructure is $P = 1100$ nm and width of corrugations is $W = 650$ nm. (b) Top: two-channel microfluidic chip consisting of the nanostructured plasmonic surface, a double-sided adhesive layer which is patterned to form the fluidic channels on top of the nanostructured surface, a poly(methyl methacrylate) layer on top, and its input and waste removal tubing. Bottom: cross-sectional scanning electron micrograph of the fabricated sensor (scale bar, $2 \mu\text{m}$). (c) Calculated electric field distribution and field lines for localized plasmon and surface plasmon resonances (scale bar, 200 nm). (d) Schematic showing a typical output of the platform during a multistep detection experiment, which shows a resonance shift value specific to surface layer formation, bulk RI value at each step, and the thickness of different layers formed on top of the sensor surface.

precise mechanical movement control. There have been other efforts for surface layer thickness measurements. For example, dielectric microresonators were suggested for thickness determination with sub-nanometer precision.¹⁹ In another research, this was achieved using localized plasmon resonances of gold nanocrescents.²⁰ These platforms usually require complex optical spectroscopy at wavelengths above $1 \mu\text{m}$ and also require advanced nanofabrication techniques, limiting the broad applicability of these sensors. In addition, for the ring resonator case, the area of a single sensing site is about $50 \mu\text{m}^2$.

From the detection perspective, sensing based on RI variations is prone to both nonspecific binding and undesired signal variations due to high changes in background RI. Whereas prism-based plasmonic sensors are more sensitive to RI variations compared to their nanoplasmonic counterparts, they are also more vulnerable to undesired signal variations originating far from the surface. Hence, several referencing techniques have been proposed to address this challenge and to provide real-time insight into binding dynamics.^{21–27}

In this article, we introduce a dual-mode plasmonic sensor based on entangled Fabry–Perot cavities (EFPC) that both eliminates background RI variations and provides thickness of the surface-adsorbed layers. Fabrication of the structure is based on well-established large-area photolithography, which substantially reduces the costs of producing sensing chips

compared to processes based on e-beam lithography. In addition, measurement setup is based on a portable spectrometer at visible wavelengths, which minimizes costs of the measurement system. By providing the aforementioned features, the presented device has the potential to be widely used in both biological research laboratories and settings with limited resources available.

RESULTS AND DISCUSSION

A plasmonic surface relief grating can be tailored in order to exhibit two modes with characteristics of surface plasmon (SP) polaritons and localized plasmon (LP) resonances (Figure 1a). A well-established optical lithography procedure is used to fabricate the nanostructured metallic surface, and the measurement setup is kept uncomplicated. Figure 1b shows a two-channel microfluidic device (top) fabricated on top of the sensor surface and a scanning electron micrograph (bottom) from a cross section of the nanostructure. Figure 1c shows field profiles for its SP (top) and LP (bottom) resonances. We performed numerical analysis to show that the structure can be modeled as two entangled Fabry–Perot cavities in a free-space optics configuration. We present a simple yet effective algorithm for estimating thickness of the surface-adsorbed layer by tracking resonance wavelengths of the dual-mode sensor. Performance of the device is tested for estimating thickness of homogeneous adsorbed layers. The sensor's

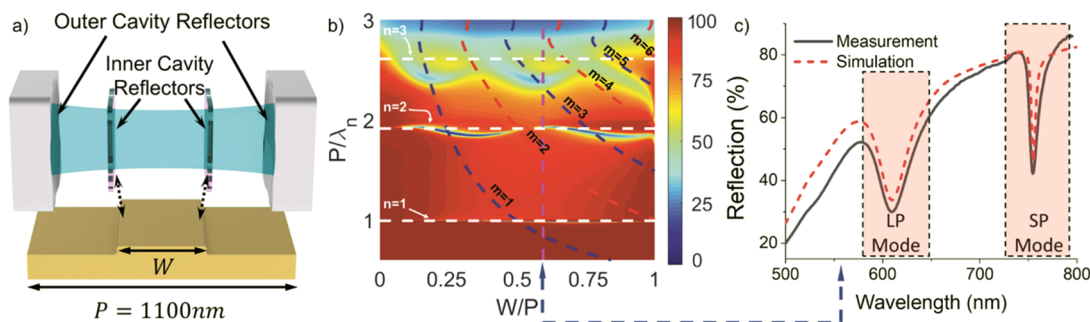


Figure 2. Theoretical modeling, numerical calculations, and experimental evaluation of the plasmonic Fabry–Perot cavities. (a) Unit cell of the corrugated gold surface (bottom), which can be modeled as two free-space entangled Fabry–Perot cavities (top). (b) Calculated zeroth order reflection from the plasmonic surface with a period of $P = 1100$ nm for different normalized frequencies P/λ_n ($\lambda_n = \lambda_0/1.33$ is the light wavelength in water) and different strip width to periodicity ratios W/P . White horizontal dashed lines show the surface plasmon resonance condition of different orders (n). Blue and red dashed lines, respectively, show odd and even orders (m) of the surface plasmon cavity formed by the edges of the corrugations. Pink vertical dashed line represents the selected W/P for dual-mode plasmonic sensing. (c) Calculated and measured reflection spectra for the corrugated metallic surface for the selected W/P ($W = 650$ nm).

responses to bulk RI variations, formation of a protein layer on top of the sensor surface, and adsorption of exosomes to the surface agree well with predictions of our numerical analysis. We provide a detailed numerical analysis on the possibility of extending application of the algorithm in estimating thickness of surface-adsorbed layers with nonhomogeneous geometry. As the schematic in Figure 1d summarizes, the device can provide an estimate on the thickness of adsorbed layers and differentiate variations of background RI from binding events.

Entangled Fabry–Perot Cavities. Surface plasmons propagate on the interface of metal and dielectric media with an effective index, which is higher than the RI of the dielectric. A periodic metallic surface of period P exposed to a normal TM-polarized plane wave may exhibit plasmonic resonances if the well-known phase match condition of

$$k_g = k_0 n_{\text{SP}} \quad (1)$$

is met. In this equation, k_0 is the free-space wavenumber, $k_g = \frac{2n\pi}{P}$ is the grating wavenumber of order n , and

$$n_{\text{SP}} = \mathcal{R} \left\{ \sqrt{\frac{\epsilon_m \epsilon_d}{\epsilon_m + \epsilon_d}} \right\}$$

is the effective index of surface plasmons on a flat metallic surface, where ϵ_m is the complex permittivity of the metal and ϵ_d is that of the dielectric medium. For the structure of Figure 2a (bottom), surface waves once excited will propagate undisturbed until being partially reflected at either edge of the surface reliefs. These two partial reflectors form a Fabry–Perot (FP) cavity of length W for the excited surface plasmons. The situation is similar to a free-space optics problem of two EFPC (Figure 2a, top), where the outer cavity models the surface plasmon excitation condition and the inner cavity stands for the plasmonic FP cavity formed by the edges of metallic corrugations. The resonance condition for the inner cavity can be expressed as

$$k_0 n_{\text{SP}} W = m\pi \quad (2)$$

In this equation, m is the resonance order for the cavity. In Figure S1, we compared reflection from the corrugated metallic surface with that of a free-space EFPC configuration in order to show their similar behavior. Figure 2b shows the reflection spectra for a gold grating calculated using the transmission-line formulation (TLF) method,^{28–30} with its vertical axis showing the normalized frequency P/λ_n and the horizontal axis representing the ratio of its corrugations' width to its

periodicity W/P . In our design, the grating height is set to 35 nm and periodicity is 1.1 μm to provide resonances at wavelengths below 800 nm.

We selected a strip width of $W = 650$ nm ($W/P = 0.59$) for our sensor, as shown with a pink vertical dashed line in Figure 2b, to achieve two resonances with those two distinct field profiles, as was shown in Figure 1c. This wavelength range features well-established inexpensive spectroscopy devices and enables portable point-of-care measurements. As Figure 2b presents, the resonance at $P/\lambda_n = 1.94$ ($\lambda_0 = 755$ nm) is barely affected by the inner cavity and occurs almost exactly where the surface plasmon resonance condition of eq 1 is satisfied (white dashed line with $n = 2$ in Figure 2b). This resonance exhibits a large evanescent tail (Figure 1c, bottom) and shares other features with surface plasmon resonances. On the other hand, the resonance at $P/\lambda_n = 2.4$ ($\lambda_0 = 610$ nm) occurs when the FP resonance condition of eq 2 with $m = 3$ is fulfilled (blue dashed line with $m = 3$ in Figure 2b). Due to the strong coupling of surface plasmons to plasmonic FP cavity at this resonance, the resonance frequency is largely deviated from the predictions of eq 1. The same phenomenon happens in the free-space optics configuration of the EFPC model, as depicted in Figure S1a. The field profile of this mode decays very rapidly (Figure 1c, top) thanks to the strong field enhancement inside the inner FP cavity. This resonance is similar to a LP resonance, which is intrinsic to metallic nanoparticles. Figure 2c compares calculated zeroth order reflection from the plasmonic surface (normalized to reflection from a gold mirror) with measured values of reflection from a fabricated sample. Both curves share the same behavior, and the resonances occur exactly at the predicted wavelengths, confirming the accuracy of our analysis and design process.

Theoretical Basis of Surface Layer Detection and Characterization. When a biolayer adsorbs to the sensor surface, the effective RI in the vicinity of the surface increases, resulting in the red shifts of the resonance wavelengths. In conventional plasmonic biosensing, the resonance shift is attributed to binding of the surface-adsorbed layer. However, from the value of the shift itself, it is indiscernible whether a thick layer with low RI has been formed on the surface or the shift is due to formation of a thin layer with higher RI. In addition, conventional plasmonic sensors usually use an additional measurement on a reference channel to eliminate bulk RI variations.³¹ In the previous section, we discussed that

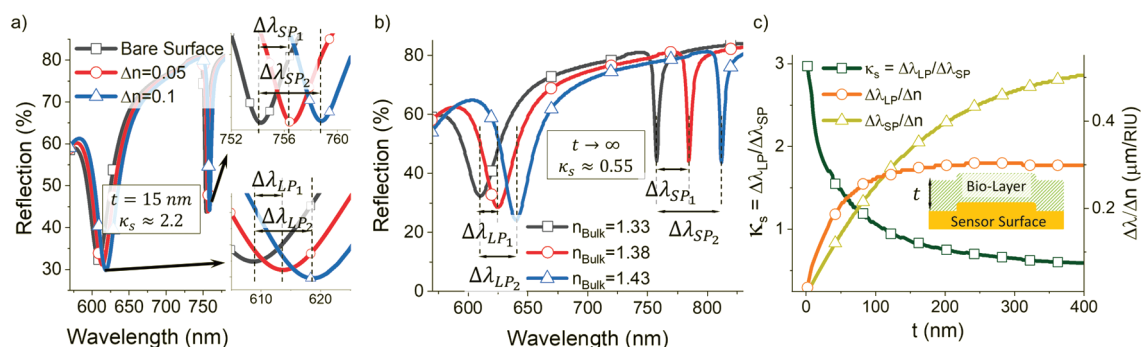


Figure 3. Theoretical basis of plasmonic thickness measurement. (a) Calculated reflection from the structure for the bare surface (square markers), when a 15 nm thick layer of RI $n = 1.38$ is formed on the surface (round markers) and when the RI of the same layer is $n = 1.43$ (triangular marker). The calculated wavelength shift ratio ($\kappa_s = \Delta\lambda_{LP}/\Delta\lambda_{SP}$) in both cases is $\kappa_s = 2.2$. (b) Calculated reflection from the structure when the sensor surface is completely surrounded by an infinite layer with RI of $n = 1.33$ (square markers), $n = 1.38$ (round markers), and $n = 1.43$ (triangular markers). Wavelength shift ratio in both cases remains around $\kappa_s = 0.55$. In (a,b), the ratio of the resonance shift remains almost constant, but the magnitude of the shifts is proportional to RI of the surface layer. (c) Calculated wavelength shifts of the LP and SP resonances (right axis) and their ratio (left axis) for different surface layer thicknesses (t). In this calculation, RI of the adsorbed layer is $n = 1.38$ ($\Delta n = 0.05$), and the shift values are normalized to Δn .

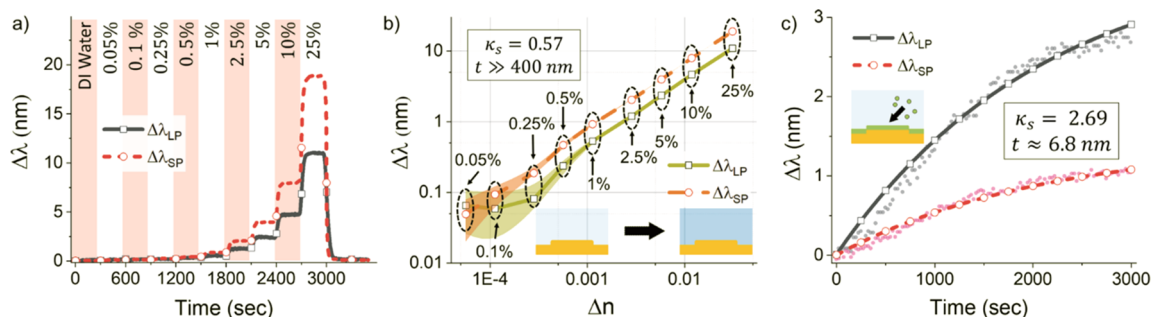


Figure 4. Sensor response to the bulk RI variation and surface adsorption. (a) Measured shift values for the LP and SP resonances over time, while aqueous glycerol solutions of increasing volumetric concentrations ($C_{\text{volumetric}} = 0, 0.05, 0.1, 0.25, 0.5, 1, 2.5, 5, 10, 25\%$) were consecutively flowed inside a microfluidic channel fabricated on top of the plasmonic surface. (b) Measured value of resonance shifts for the aqueous glycerol solutions of (a) shown as a function of RI increment. Shaded regions around the curves show the error bounds for the measured shift values. (c) Measured values for the resonance shift and corresponding isotherm curves fitted to the data over time, while a NeutrAvidin (50 $\mu\text{g}/\text{mL}$ in phosphate-buffered saline) layer binds to the surface. By passing glycerol solutions of different concentrations in (a), the wavelength shift ratio remains at around $\kappa_s = 0.57$, which is in agreement with our calculations for bulk RI variations. For the binding of neutravidin in (c), the measured value of the wavelength shift ratio is $\kappa_s = 2.69$, corresponding to the formation of a 6.8 nm thick adsorbed layer.

the LP and SP modes show distinct field profiles around the sensing surface. We here show that this feature can be utilized to estimate the thickness of the surface-adsorbed layer and to distinguish bulk and surface variations. In our approach, there would be no need for a measurement from an additional reference channel for eliminating bulk effects.

Figure 3a presents the simulation results for reflection spectra for the bare sensor surface and when a 15 nm thick layer with RI of either $n = 1.38$ ($\Delta n = 0.05$) or $n = 1.43$ ($\Delta n = 0.1$) is present on the sensor surface. Figure 3b shows reflection spectra for layers with the same values of RI but infinite thickness. Although the amount of the shifts for LP and SP resonances increases with an increase in the RI of the surface layer, the ratio of the shifts $\kappa_s = \Delta\lambda_{LP}/\Delta\lambda_{SP}$ remains almost constant. This ratio does not vary with RI (only slight variations of up to 2% for a large RI change of $\Delta n = 0.1$ RIU), but it varies mainly with thickness of the surface-adsorbed layer. For the 15 nm thick layer of Figure 3a, the ratio is $\kappa_s = 2.2$, and for the layer of infinite thickness, it is $\kappa_s = 0.55$. Figure 3c shows the magnitude of the wavelength shifts and the shift ratio for surface layers with thicknesses of $0 < t \leq 400$ nm and

RI $n = 1.38$. Using the data of Figure 3c, it is possible to estimate the thickness of surface-adsorbed layers by calculating the wavelength shift ratio during an experiment. The wavelength shift ratio is around 3 for layers with a few nanometer thicknesses and it drops to 0.59 for the 400 nm thick layer. In addition to surface layer characterization, the ratio κ_s can be used as a reference in order to eliminate variations in the RI of background solution when different fluids are flowed over the sensor. For example, when a fluid containing analytes is injected to a sensor channel that is preoccupied by a different fluid with different RI, first there would be sudden resonance wavelength changes with $\kappa_s \approx 0.55$. Then, during adsorption of the analyte to the surface, the resonances will shift more. Whereas the value of κ_s at the beginning of any new injection corresponds to bulk variation, its value during the binding step can be used to estimate the thickness of the adsorbed layer. However, if bulk RI changes and binding of analytes occurs concurrently with a similar rate, for example, as a result of a temperature drift during the surface adsorption, estimating the thickness of the adsorbed layer using the wavelength shift ratio κ_s would be erroneous. Hence,

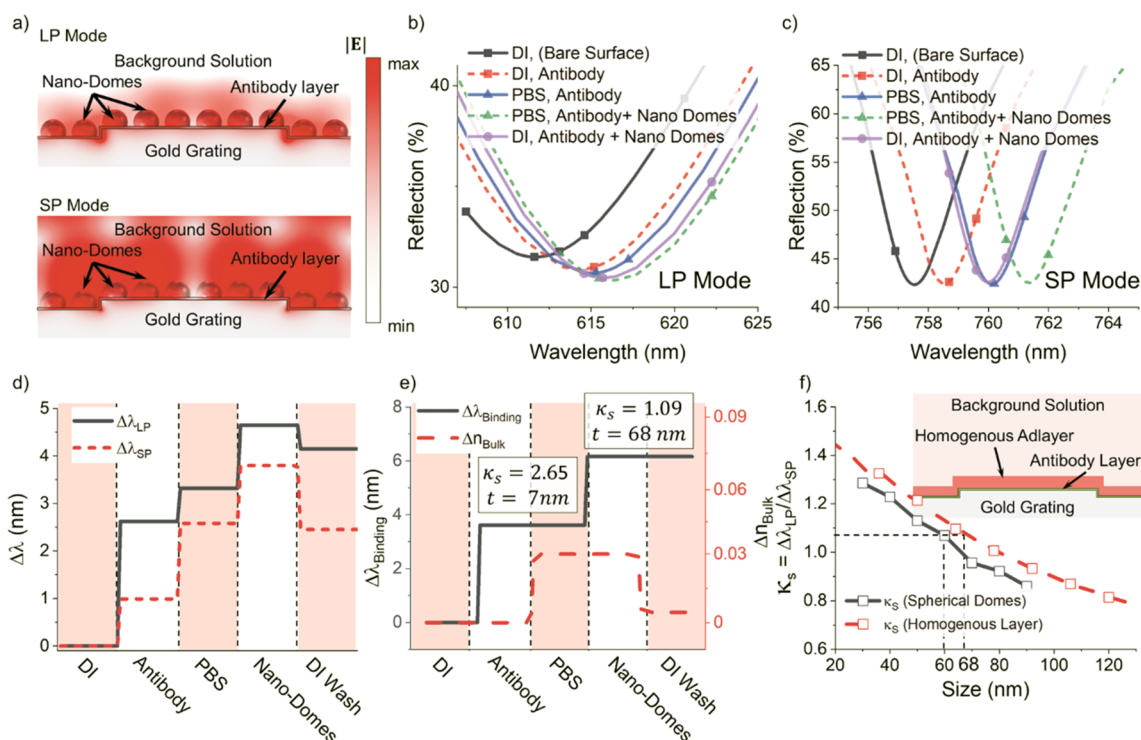


Figure 5. Thickness estimation for spherical dome-shaped analytes. (a) Field distribution for the LP (top) and the SP modes (bottom) when dome-shaped analytes cover an antibody-coated sensor surface. The antibody layer is modeled as a homogeneous 7 nm thick layer with RI of $n_{ab} = 1.38$. The analytes are modeled by spherical domes of height 60 nm and RI $n_d = 1.35$. Calculated reflection spectra near LP (b) and SP (c) resonance wavelengths for (i) the bare surface immersed in DI water ($n_B = 1.33$), (ii) a sensor surface covered with antibody and DI as the background solution, (iii) a surface covered with antibody and PBS ($n_B = 1.333$) as the background, (iv) nanodomains adsorbed to the antibody coated sensor and PBS as the background, and (v) the same configuration but with DI as the background. (d) Shift values of resonance wavelengths for each of the five different configurations. (e) Left axis shows the binding portion of total wavelength shift ($\Delta\lambda_{\text{LP}} + \Delta\lambda_{\text{SP}}$) differentiated from wavelength shifts resulting from bulk RI variations. Right axis shows bulk RI at each step, which is calculated from the remaining part of the resonance shifts. Wavelength shift ratio for the antibody layer is $\kappa_s = 2.65$, and for dome-shaped analytes, it is $\kappa_s = 1.09$. (f) Calculated wavelength shift ratio κ_s for adsorbed layers consisting of nanometric spherical domes of different sizes (solid black line) and for homogeneous layers of different thicknesses (dashed red line). Inset shows a schematic of the homogeneous adsorbed layer. For the spherical domes shown in (a), the homogeneous adsorbed layer model estimates a thickness of 68 nm, and the spherical dome model accurately estimates its size to be 60 nm.

for the best estimate on the thickness, temperature drift during experiments should be avoided.

Sensor Characterization. Performance of the fabricated sensor chips was examined in a series of experiments. First, bulk sensitivity of the sensor was investigated by applying aqueous glycerol solutions of different concentrations to the sensor. The collected reflection spectrum was analyzed to find the reflection minima of LP and SP resonances. Figure 4a shows the resonance shifts over time during the experiment. As the results demonstrate, the more bulk sensitive SP resonance shifts more than the LP resonance. Figure 4b represents the values of the measured resonance shifts and its associated readout noise in the RI range of $1.33 < \Delta n < 1.48$. It is seen that the SP resonance can be used to detect bulk RI variations with a resolution better than 1×10^{-4} RIU, and the LP resonance can be used for RI variations larger than 5×10^{-4} RIU. The higher performance of SP resonance in bulk RI detection is due to its extended range of field profile well inside the solution, as shown in Figure 1c. The situation is completely reverse when we examine the performance of the sensor in the detection of surface adsorption during binding of NeutrAvidin to a gold surface prefucosylated with a DSP cross-linker (see Materials and Methods for the details of the functionalization). Figure 4c shows the measured values of resonance shifts over

time and the fitted Langmuir isotherm curves. Unlike bulk RI sensing, in this experiment, the LP resonance shifts more and shows superior performance in a single-mode sensing aimed at detection of surface binding events. By tracking both resonances over time in a dual-mode sensing strategy and with the help of simulations summarized in Figure 3c, the platform gives an estimate on the thickness of the adsorbed layer and distinguishes bulk variations from surface events. Based on Figure 3c, any wavelength shift ratio smaller than $\kappa_s < 0.59$ corresponds to formation of a layer thicker than 400 nm and is attributed to bulk RI variation. For the resonance shifts demonstrated in Figure 4b, this ratio is $\kappa_s = 0.57$, confirming bulk RI variation. That ratio for the NeutrAvidin experiment shown in Figure 4c is $\kappa_s = 2.69$. Based on Figure 3c, this value corresponds to formation of a layer with the thickness of about 6.8 nm. This estimation is in agreement with previous studies based on X-ray measurements, suggesting a range from 4 to 8 nm for dimensions of avidin molecules.^{32,33}

By taking into account the magnitude of the noise in our readout system, the resolution of our spectrometer, and the unpredictability that happens due to the slight variations in κ_s ratio for layers of the same thickness but different RI, our calculation shows that the error in thickness determination using the platform is less than 4 nm for layer thicknesses

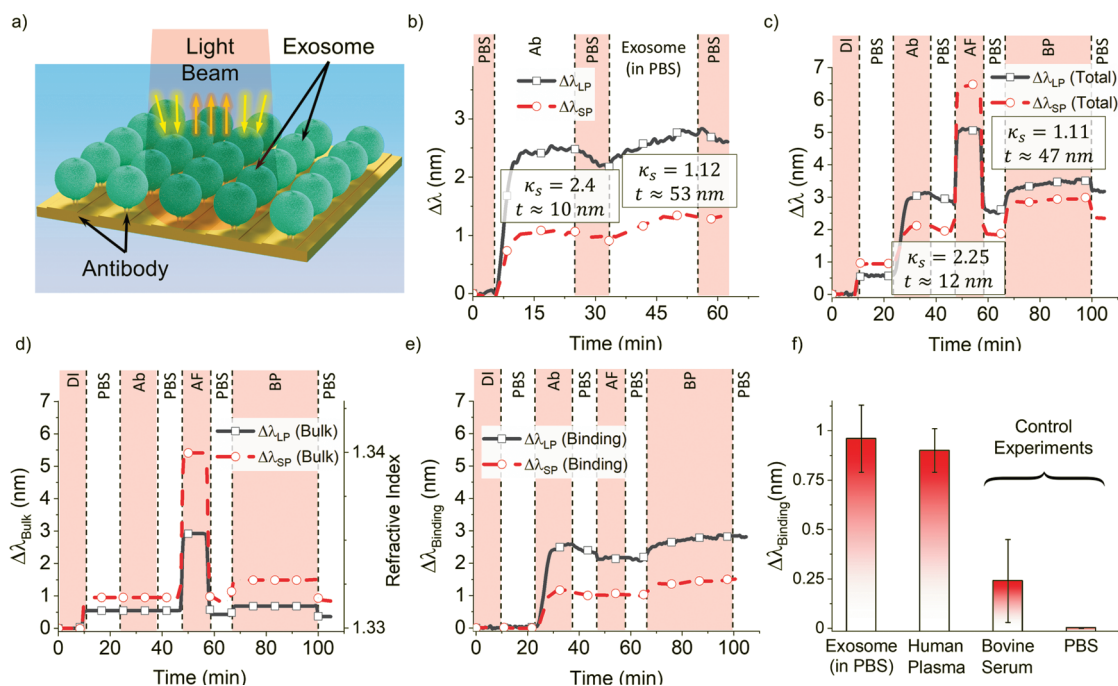


Figure 6. Exosome detection and size estimation. (a) Schematic presentation of an antibody-coated EFPC structure illuminated by incident light beam during a vesicle detection experiment. (b) Measured shift values for the LP ($\Delta\lambda_{LP}$) and SP resonances ($\Delta\lambda_{SP}$) during detection of exosomes spiked in PBS. Each step is labeled at the top of the figure. The ratio of resonance shifts due to binding of antibody is $\kappa_s = 2.4$ and its value for binding of exosomes to the surface is $\kappa_s = 1.12$. These values correspond to the formation of 10 and 53 nm thick layers, respectively. (c) Shift values for the LP and SP resonances during an experiment on diluted healthy human plasma (1:10). Human plasma has exosomes in it. The experiment consists of eight binding and washing steps that are labeled at the top (AF, antifouling agent; BP, diluted healthy human blood plasma (1:10) that includes exosomes). The ratio of resonance shifts for the antibody layer after the application of antifouling agent is $\kappa_s = 2.25$ and for the human plasma step is $\kappa_s = 1.11$. These values correspond to formation of a 12 nm thick antibody layer and a 47 nm thick analyte layer. In the following two plots, we portioned the resonance shifts into bulk and binding parts. (d) Portion of the LP and SP resonance shifts attributed to the bulk refractive index variations during the experiment. The curve for SP resonance shift (red dashed line) additionally shows RI of the background solution indicated on the right axis. (e) Remaining portion of the resonance shifts owing to binding events. (f) Total resonance shifts ($\Delta\lambda_{SP} + \Delta\lambda_{LP}$) after binding of extracted human exosomes spiked in PBS (1×10^{10} particles/mL), diluted healthy human plasma (1:10), diluted bovine serum (1:10, negative control), and application of PBS. The sensor surface was decorated up to the Ab layer, followed by the binding of antifouling agent. The data represent mean value and standard deviation over repeated experiments ($N = 2-6$).

between 10 and 100 nm. For thicker layers with thicknesses of up to 400 nm, the error is less than 4%. Thickness measurement could become inaccurate for layers thinner than 10 nm due to limited spectral resolution of the spectrometer and the inaccuracy in determining the shift magnitude. Hence, the platform is well-suited for characterization of layers with their thickness between 10 and 400 nm. This range covers many biotargets such as most viruses, cellular secreted particles, proteins, and liposomes.

We further theoretically tested the limits of the sensor system, and our findings suggest that the sizing algorithm can be extended to estimate the thickness of layers with more complex geometry, with spherical targets binding to the sensor surfaces rather than homogeneous layers of proteins coating the sensor surfaces. In this regard, we first calculated the sensor response to formation of an antibody layer modeled as a homogeneous layer with a thickness of 7 nm and RI of $n_{ab} = 1.38$. Then, we calculated its response to adsorption of nanometric domes with a height of 60 nm and RI of $n = 1.35$. In this simulation, nanodomains are spheres cut off by a horizontal plane with their diameter 1.5 times their height (see Figure 5a). They are used to model typical cellular entities as many cellular entities such as extracellular vesicles⁹ or many viruses³⁴ are spherical in character and do not always fully coat

a sensor surface. The size of 60 nm is chosen to reflect the average size of extracellular vesicle or a virus (see the Materials and Methods section for the details of the simulation). Figure 5a shows the configuration and the field distributions for the LP (top) and the SP resonances (bottom). Figure 5b,c, respectively, shows calculated reflection spectra near LP and SP resonances for five different configurations: (i) a bare sensor is immersed in deionized (DI) water ($n_B = 1.33$); (ii) a homogeneous layer of antibody covers the surface and the background solution remains as DI water; (iii) RI of background solution increases due to introduction of phosphate-buffered saline (PBS) to the sensor ($n_B = 1.333$); (iv) 60 nm high dome-shaped analytes cover the surface while RI of background solution remains at $n_B = 1.333$; and (v) same configuration as (iv) but with DI water ($n_B = 1.33$) as the background solution. The values of resonance shift for these steps are summarized in Figure 5d. We used wavelength shift ratio κ_s for each step in order to distinguish bulk RI variations from binding events. The left axis in Figure 5e shows the binding-related portion of total resonance shift, and its right axis shows the calculated RI of the background solution. The wavelength shift ratio can be also used to estimate the thickness of each of the layers formed on top of the surface. For the step (ii), in which the homogeneous protein layer was

placed on the sensor surface, the calculated shift ratio is $\kappa_s = 2.65$. Based on the data of Figure 3c, this value corresponds to formation of a 7 nm thick layer. For estimating the thickness of the secondary adsorbed layer of step (v), we first calculate the relation between the wavelength shift ratio and the thickness of a secondary adsorbed layer formed on top of the 7 nm thick antibody layer (Figure S3). Figure 5f shows the wavelength shift ratio calculated for homogeneous secondary adsorbed layers of different heights (dashed line) and nonhomogeneous secondary adsorbed layers consisting of dome-shaped analytes (solid line). As shown in Figure 5e, the calculated shift ratio for the secondary adsorbed layer of step (v) is $\kappa_s = 1.09$. For this value of κ_s , the homogeneous model (dashed line) estimates a thickness of 68 nm, which is 8 nm larger than the actual heights of the nanometric domes used in the simulation model. On the other hand, the solid line in Figure 5f gives an accurate size estimate for adsorption of nanodomains in step (v). This shows that a prior knowledge on the geometry of the biotargets in a detection experiment can be useful in improving the accuracy of thickness estimation algorithm. For this purpose, we first need to perform simulations to find the relation between the wavelength shift ratio and the size of the nano-objects of known geometry and then use its results and the measured wavelength shift ratio to estimate the size of the objects.

We also used biological samples to evaluate the performance of the implemented system for the detection of human exosomes. For this purpose, first, the sensor surface is functionalized with mouse anti-human monoclonal CD63 antibodies (Ab), specific to one of the most abundant tetraspanins on exosome surfaces (*i.e.*, CD63). Then, exosomes isolated from a human breast cancer cell line (MDA-MB-231) were spiked into PBS (1×10^{10} particle/mL) and injected to the chip.³⁵ Figure 6a shows a schematic of the experiment, and Figure 6b demonstrates the measured resonance shifts during this experiment. Accordingly, the wavelength shift ratio for antibody binding step is $\kappa_s = 2.4$, which corresponds to the formation of a layer with a thickness of $t \approx 10$ nm. The ratio for the binding of exosomes is $\kappa_s = 1.12$, which corresponds to the formation of a secondary adsorbed layer with a thickness of $t \approx 53$ nm. This is within the range of the reported exosome sizes in the literature and our measurements (Figure S4) using nanoparticle tracking analysis.³⁵

In the next experiment, we examined the performance of the platform in detecting extracellular vesicles from plasma of a healthy individual. In order to minimize nonspecific binding, an antifouling agent was applied to the sensor, followed by passing human plasma diluted in PBS (1:10) over the surface. The channel was then washed by injection of PBS. Figure 6c shows the shifts of the resonances during the experiment. For the bulk RI variations, the SP resonance shifted more than the LP resonance. On the other hand, for binding events, the LP resonance usually resulted in larger shifts. Hence, the shift ratio κ_s was to distinguish the surface binding events from the bulk RI variations. It is important to note that there are situations where bulk RI variation and binding of analytes to the surface occur simultaneously. As shown in Figure 6c, the application of diluted human plasma to the sensor led to an abrupt shift in the resonance wavelengths. The measured value of wavelength shift ratio for this abrupt resonance shift is larger than that of a pure bulk RI variation (Figure S5), indicating that both binding of analytes and variations in bulk RI occur simultaneously during this period. In order to differentiate

the portion of resonance shifts due to the bulk RI variation from that of surface binding in real time, we assumed that the thickness of the analyte layer is similar to the thickness of the exosome layer (*i.e.*, $\kappa_s = 1.12$). This differentiation can be adjusted later using the measured value of κ_s calculated after washing the surface with PBS (as shown in Figure 6c). In Figure 6d, the portion of resonance shifts due to the variations of background RI is shown. Here, the red dashed curve represents both the SP resonance shift (corresponding to the left axis) and RI of the background solution (corresponding to the right axis). Figure 6e shows the portion of resonance shifts owing to the binding events. The measured wavelength shift ratio after applying antifouling agent to the sensor surface coated with an antibody layer is $\kappa_s = 2.25$. This ratio is $\kappa_s = 1.11$ for the formation of the analyte layer. These values correspond to formation of a 12 nm thick antibody layer and a 47 nm thick analyte layer (Figure S5).

Fetal bovine serum (FBS) is used as a negative control. FBS includes the exosomes with bovine CD63 surface markers that do not specifically get captured by anti-human CD63 antibodies. FBS was diluted in PBS (1:10) and applied to the sensor surface decorated with anti-human CD63 antibodies. Figure 6f shows the average value and deviation of total resonance shift ($\Delta\lambda_{LP} + \Delta\lambda_{SP}$) on repeated trials ($N = 2-6$) for the isolated exosomes, human blood plasma, FBS, and PBS after the application of antifouling agent. We observed large resonance shifts for both the cancer-cell-derived exosomes and healthy human plasma exosomes, but resonance shift was very low for the FBS. This observation confirms the minimal effect of nonspecific binding due to the presence of an antifouling agent and successful detection of exosomes with the presented platform.

CONCLUSIONS

Here, we show that by selecting proper values for its periodicity, width, and height, a corrugated metallic surface can provide surface layer sizing and differentiating background RI variations from the binding events by the distinct field profiles of the LP and SP modes. The accuracy of the implemented algorithm in determining the RI of background solutions and the thickness of a homogeneous surface-adsorbed layer is evaluated by rigorously assessing possible sources of error in both the measurement setup and the algorithm. Our EFPC structure effectively enables sizing of layers with thicknesses between 10 and 400 nm and can detect background RI variations of less than 1×10^{-4} RIU. Employing low-noise and high-dynamic-range photodiode arrays instead of the portable spectrometer would greatly enhance both detection limit and size detection accuracy. We also evaluated the accuracy of the method in determining the thickness of nonhomogeneous adsorbed layers by performing numerical simulations, taking geometry of a typical analyte into account. Those simulations can be used to improve accuracy of the thickness estimation algorithm for nonhomogeneous adsorbed layers. In addition, performance of the sensor in estimating the thickness of a layer formed by binding of NeutrAvidin molecules was experimentally demonstrated. Our estimate on the thickness of the NeutrAvidin layer is in good agreement with the previous reports on dimensions of the molecule based on X-ray measurements. The presented results for exosome detection experiments once again confirm that the proposed technique can distinguish bulk RI variations and provide insight into binding dynamics, value of background RI,

and, most importantly, an estimate on the thickness of the adsorbed layer. It is noteworthy that field magnitude at both resonances of the structure decays in the direction normal to the surface, but it is periodic in the horizontal plane. Hence, when analytes partially cover the surface, the resulting ensemble response can be modeled with a layer with the same height as analytes but with an effective RI lower than the analyte. In other words, although each resonance shift is related to surface concentration of the analyte,³⁶ the shift ratio varies mainly with thickness of the analyte layer. Detection and size estimation for analytes of very low concentrations could become inaccurate due to limited performance of the portable spectrometer. Employing photodiode arrays would be useful for such experiments. On the other hand, for analytes of very high concentration, the measurement setup can be simplified by tracking light intensity at only a few discrete wavelengths instead of using a spectrometer. This approach decreases accuracy of the detection and size estimation, but it reduces the costs further and provides detection and size estimation for a wide range of applications in nanosensing. Nonspecific binding may lower performance of the detection and size estimation. Bulk RI variations, if they occur slowly during a binding step, will decrease the accuracy of the results. This can be avoided in most cases by controlling the temperature of the sensor. Possible variations in geometry of the structure, which may occur due to uncertainties in fabrication process or degradation of the nanostructure over long periods of time, may enforce additional calibration steps upon testing. A rapid calibration can be performed by measuring the response of the sensor to injection of liquids with different RI. For analytes with a RI similar to the background solution, resonance shifts will be very small and the detection may become inaccurate. To provide a higher RI contrast, it is possible to inject a fluid with different RI once the analyte layer is formed. Although well-established techniques such as dynamic light scattering provide information about size distribution of the biotarget particles inside a solution,³⁷ the proposed technique in this work provides the average size of the analytes only after their binding to the sensing surface using the ensemble response resulting from their adsorption. Nonetheless, the EFPC structure can provide a complementary alternative for determining and comparing the size of biotargets from different samples.

Apart from the dual-mode sensing approach for surface layer thickness measurement, the LP and SP resonances can be used to simultaneously detect biotargets of different size on the same surface. In this strategy, due to their different decay rate of the evanescent electric field, the LP resonance is mostly useful for the targets of smaller sizes (less than 100 nm) and SP resonance will be mostly sensitive to binding of larger biotargets (larger than 50 nm). This strategy should involve functionalizing the surface with antibodies for the different targets of interest. The specificity of the used capture moieties is an important parameter to capture, detect and quantify the target structures in heterogeneous solutions. Another approach is to use the device integrated with an imaging setup. In addition to the thickness estimation algorithm, the introduced model based on entangled Fabry–Perot cavities would be useful in understanding the behavior of the reflective metallic surfaces and has the potential for application in biosensing.

MATERIALS AND METHODS

Gold Sensor Fabrication. Five nanometers of titanium and 160 nm of gold were deposited on silicon wafers using an AJA evaporator system. Then a 0.7 μm thick layer of the Megaposit SPR 955 positive photoresist was spin-coated on top of the wafers. A photomask for the line array was designed with an equivalent line width of 450 nm and periodicity of 1100 nm and fabricated on a quartz substrate using electron beam lithography. The mask was used twice for wafer exposure using Stanford's ASML PAS 5500/60 i-line stepper. The wafers were shifted for 200 nm between the exposures to produce the desired 650 nm line width. After the photoresist was developed, 35 nm of gold was deposited on top of the wafers, and the process was concluded by stripping the remaining unexposed resist and further cleaning.

Microfluidic Chip Fabrication. The microfluidic chips were made by connecting a 3.2 mm thick poly(methyl methacrylate) (PMMA) sheet to the nanostructure sensing surfaces using a patterned double-sided adhesive (DSA) film with 50 μm thickness as described earlier.³⁸ Versa LASER (Universal Laser Systems Inc., Scottsdale, AZ) was used to cut the PMMA layer and DSA film to form the channel, inlets, and outlets. Proper tubing was then performed and sealed *via* a liquid epoxy.³⁹

Surface Chemistry and Measurement Procedures. For all of the experiments involving surface layer detection, we functionalized gold surfaces by incubating the nanostructured sensors in a solution of DSP (Lomant's reagent) and DMSO overnight at room temperature. After the gold surfaces were washed with DI water, microfluidic chips were assembled on top of the sensing surface and the tubing was performed. After this step, the sensor surface was decorated with either NeutrAvidin or antibody. A protein-free blocking buffer (Pierce) was used in human plasma and bovine serum experiments. Injection rate for washing steps was set to 5 $\mu\text{L}/\text{min}$, and for binding steps, it was reduced to 2.5 $\mu\text{L}/\text{min}$.

Measurement Setup. The output white light of a Thorlabs OSL2 light source was delivered to the sample by means of an optical fiber. The light was then collimated and polarized before passing through a nonpolarizing beam splitter and illuminating the sensor. The reflected light was passed through the beam splitter again and was collected using a fiber coupling lens and transferred to a portable optical spectrometer (HR2000+, Ocean Optics). A gold mirror was used to calibrate the magnitude of the recorded spectrum.

Exosome Preparation. The MDA-MB-231 cell line was cultured in Dulbecco's modified Eagle medium (DMEM) supplemented with FBS (10%) at 37 °C in 5% CO₂ until the culture reached confluency. After confluency, the culture was washed with PBS three times to remove the remaining culture media in the flask, and a fresh culture media prepared with DMEM supplemented and exosome-depleted FBS (5%) were used to culture cells for an additional 48 h. After this period, culture medium was collected from the flasks and centrifuged at 2000g at 4 °C for 20 min to separate cells, cell debris, and larger contaminating particles. The supernatant after centrifugation was utilized for exosome isolation. We used ExoTIC, an in-house developed platform, to isolate exosomes. ExoTIC is a mechanical filtration-based size-sorting technology as earlier reported in detail.^{35,40} Human plasma samples were prepared from the healthy whole blood samples obtained from Stanford Blood Center in purple top blood collection tubes with K₂EDTA and diluted (1:10) with PBS to use in the experiments.

Plasmonic Simulations. A MATLAB program was developed based on the TLF method. Detailed descriptions on this method and its implementation can be found elsewhere.^{28–30} The TLF method was used for all two-dimensional simulations. We modeled the gold layer using experimental data for its complex dielectric function.⁴¹ To account for surface functionalization with Lomant's reagent, a 2 nm conformal dielectric layer was used in simulations. Simulations for dome-shaped analytes were performed using the electromagnetic waves module of COMSOL Multiphysics. For this purpose, periodic boundary conditions were used at the boundaries of the unit cell, and the structure was illuminated by a plane wave through a periodic port.

ASSOCIATED CONTENT

Supporting Information

The Supporting Information is available free of charge at <https://pubs.acs.org/doi/10.1021/acsnano.0c02797>.

Additional details on the entangled Fabry–Perot cavity model, comparison of reflection maps for free-space and plasmonic entangled Fabry–Perot cavities, steps of nanofabrication process, thickness estimation algorithm, size distribution profile of exosomes, and wavelength shift ratio for secondary adsorbed layers (PDF)

AUTHOR INFORMATION

Corresponding Authors

Mahmoud Shahabadi – Photonics Research Laboratory, Center of Excellence on Applied Electromagnetic Systems, School of Electrical and Computer Engineering, College of Engineering, University of Tehran, Tehran 1439957131, Iran; Email: shahabad@ut.ac.ir

Fatih Inci – Canary Center at Stanford for Cancer Early Detection, Bio-Acoustic MEMS in Medicine (BAMM) Laboratory, Department of Radiology, Stanford School of Medicine, Stanford University, Palo Alto, California 94304, United States; Email: finci@stanford.edu

Utkan Demirci – Canary Center at Stanford for Cancer Early Detection, Bio-Acoustic MEMS in Medicine (BAMM) Laboratory, Department of Radiology, Stanford School of Medicine, Stanford University, Palo Alto, California 94304, United States; orcid.org/0000-0003-2784-1590; Email: utkan@stanford.edu

Authors

Amideddin Mataji-Kojouri – Photonics Research Laboratory, Center of Excellence on Applied Electromagnetic Systems, School of Electrical and Computer Engineering, College of Engineering, University of Tehran, Tehran 1439957131, Iran; Canary Center at Stanford for Cancer Early Detection, Bio-Acoustic MEMS in Medicine (BAMM) Laboratory, Department of Radiology, Stanford School of Medicine, Stanford University, Palo Alto, California 94304, United States

Mehmet Ozgun Ozen – Canary Center at Stanford for Cancer Early Detection, Bio-Acoustic MEMS in Medicine (BAMM) Laboratory, Department of Radiology, Stanford School of Medicine, Stanford University, Palo Alto, California 94304, United States

Complete contact information is available at: <https://pubs.acs.org/doi/10.1021/acsnano.0c02797>

Author Contributions

All authors conceived the overall study. A.M.K. implemented the TLF method and performed the analysis and design of the nanostructure. F.I. and U.D. supervised, and A.M.K. conducted the experiments and the data analysis. M.S., F.I., U.D., and A.M.K. participated in discussions on the analysis and modeling of the sensor response. M.O.O. designed exosome capture studies and prepared biological samples. A.M.K. wrote the manuscript. All authors discussed the results and reviewed/edited the manuscript.

Notes

The authors declare the following competing financial interest(s): Prof. Utkan Demirci (UD) is a founder of and has an equity interest in: (i) DxNow Inc., a company that is developing microfluidic IVF tools and imaging technologies for

point-of-care diagnostic solutions, (ii) Koek Biotech, a company that is developing microfluidic technologies for clinical solutions, (iii) Levitas Inc., a company focusing on developing microfluidic products for sorting rare cells from liquid biopsy in cancer and other diseases, and (iv) Hillel Inc., a company bringing microfluidic cell phone tools to home settings. UD's interests were viewed and managed in accordance with the conflict of interest policies.

ACKNOWLEDGMENTS

The authors would like to thank M. Mansourpour and L. Galambos at Stanford Nanofabrication Facility (SNF) for their help in fabrication of the plasmonic devices. We also thank M. Nakamura at SNF for the fruitful discussions around designing the fabrication process. A.M.K. would like to acknowledge the office of Vice President for International Affairs from University of Tehran. A.M.K. would like to thank BAMB Lab, the Department of Radiology, Stanford University School of Medicine, for his visit where this work was performed. The authors thank Canary Center at Stanford for Cancer Early Detection seed funding for supporting this work.

REFERENCES

- (1) Tokel, O.; Inci, F.; Demirci, U. Advances in Plasmonic Technologies for Point of Care Applications. *Chem. Rev.* **2014**, *114*, 5728–5752.
- (2) Tokel, O.; Yildiz, U. H.; Inci, F.; Durmus, N. G.; Ekiz, O. O.; Turker, B.; Cetin, C.; Rao, S.; Sridhar, K.; Natarajan, N.; Shafiee, H.; Dana, A.; Demirci, U. Portable Microfluidic Integrated Plasmonic Platform for Pathogen Detection. *Sci. Rep.* **2015**, *5*, 9152.
- (3) Brolo, A. G. Plasmonics for Future Biosensors. *Nat. Photonics* **2012**, *6*, 709–713.
- (4) Cetin, A. E.; Coskun, A. F.; Galarreta, B. C.; Huang, M.; Herman, D.; Ozcan, A.; Altug, H. Handheld High-Throughput Plasmonic Biosensor Using Computational On-Chip Imaging. *Light: Sci. Appl.* **2014**, *3*, e122.
- (5) Tseng, S.-Y.; Li, S.-Y.; Yi, S.-Y.; Sun, A. Y.; Gao, D.-Y.; Wan, D. Food Quality Monitor: Paper-Based Plasmonic Sensors Prepared through Reversal Nanoimprinting for Rapid Detection of Biogenic Amine Odorants. *ACS Appl. Mater. Interfaces* **2017**, *9*, 17306–17316.
- (6) Inci, F.; Filippini, C.; Baday, M.; Ozen, M. O.; Calamak, S.; Durmus, N. G.; Wang, S. Q.; Hanhauser, E.; Hobbs, K. S.; Juillard, F.; Kuang, P. P.; Vetter, M. L.; Carocci, M.; Yamamoto, H. S.; Takagi, Y.; Yildiz, U. H.; Akin, D.; Wesemann, D. R.; Singhal, A.; Yang, P. L.; et al. Multitarget, Quantitative Nanoplasmonic Electrical Field-Enhanced Resonating Device (NE2RD) for Diagnostics. *Proc. Natl. Acad. Sci. U. S. A.* **2015**, *112*, E4354–E4363.
- (7) Tasoglu, S.; Cumhuri Tekin, H.; Inci, F.; Knowlton, S.; Wang, S. Q.; Wang-Johanning, F.; Johanning, G.; Colevas, D.; Demirci, U. Advances in Nanotechnology and Microfluidics for Human Papillomavirus Diagnostics. *Proc. IEEE* **2015**, *103*, 161–178.
- (8) Yildiz, U. H.; Inci, F.; Wang, S. Q.; Toy, M.; Tekin, H. C.; Javaid, A.; Lau, D. T. Y.; Demirci, U. Recent Advances in Micro/Nanotechnologies for Global Control of Hepatitis B Infection. *Biotechnol. Adv.* **2015**, *33*, 178–190.
- (9) Samanta, S.; Rajasingh, S.; Drosos, N.; Zhou, Z.; Dawn, B.; Rajasingh, J. Exosomes: New Molecular Targets of Diseases. *Acta Pharmacol. Sin.* **2018**, *39*, 501–513.
- (10) El Andaloussi, S.; Mäger, I.; Breakefield, X. O.; Wood, M. J. A. Extracellular Vesicles: Biology and Emerging Therapeutic Opportunities. *Nat. Rev. Drug Discovery* **2013**, *12*, 347–357.
- (11) Saeedi, S.; Israel, S.; Nagy, C.; Turecki, G. The Emerging Role of Exosomes in Mental Disorders. *Transl. Psychiatry* **2019**, *9*, 122.
- (12) Wu, R.; Gao, W.; Yao, K.; Ge, J. Roles of Exosomes Derived from Immune Cells in Cardiovascular Diseases. *Front. Immunol.* **2019**, *10*, 648.

- (13) Wu, M.; Wang, G.; Hu, W.; Yao, Y.; Yu, X. F. Emerging Roles and Therapeutic Value of Exosomes in Cancer Metastasis. *Mol. Cancer* **2019**, *18*, 53.
- (14) Tai, Y. L.; Chen, K. C.; Hsieh, J. T.; Shen, T. L. Exosomes in Cancer Development and Clinical Applications. *Cancer Sci.* **2018**, *109*, 2364–2374.
- (15) Caponnetto, F.; Manini, I.; Skrap, M.; Palmai-Pallag, T.; Di Loreto, C.; Beltrami, A. P.; Cesselli, D.; Ferrari, E. Size-Dependent Cellular Uptake of Exosomes. *Nanomedicine (N. Y., NY, U. S.)* **2017**, *13*, 1011–1020.
- (16) Sharma, S.; Gillespie, B. M.; Palanisamy, V.; Gimzewski, J. K. Quantitative Nanostructural and Single-Molecule Force Spectroscopy Biomolecular Analysis of Human-Saliva-Derived Exosomes. *Langmuir* **2011**, *27*, 14394–14400.
- (17) Yang, J. S.; Lee, J. C.; Byeon, S. K.; Rha, K. H.; Moon, M. H. Size Dependent Lipidomic Analysis of Urinary Exosomes from Patients with Prostate Cancer by Flow Field-Flow Fractionation and Nanoflow Liquid Chromatography-Tandem Mass Spectrometry. *Anal. Chem.* **2017**, *89*, 2488–2496.
- (18) Rupert, D. L. M.; Shelke, G. V.; Emilsson, G.; Claudio, V.; Block, S.; Lässer, C.; Dahlin, A.; Lötvall, J. O.; Bally, M.; Zhdanov, V. P.; Höök, F. Dual-Wavelength Surface Plasmon Resonance for Determining the Size and Concentration of Sub-Populations of Extracellular Vesicles. *Anal. Chem.* **2016**, *88*, 9980–9988.
- (19) Juan-Colás, J.; Krauss, T. F.; Johnson, S. D. Real-Time Analysis of Molecular Conformation Using Silicon Electrophotonic Biosensors. *ACS Photonics* **2017**, *4*, 2320–2326.
- (20) Abumazwed, A.; Kubo, W.; Tanaka, T.; Kirk, A. G. Improved Method for Estimating Adlayer Thickness and Bulk RI Change for Gold Nanocrescent Sensors. *Sci. Rep.* **2018**, *8*, 6683.
- (21) Homola, J.; Lu, H. B.; Nenninger, G. G.; Dostálek, J.; Yee, S. S. A Novel Multichannel Surface Plasmon Resonance Biosensor. *Sens. Actuators, B* **2001**, *76*, 403–410.
- (22) Naimushin, A. N.; Soelberg, S. D.; Nguyen, D. K.; Dunlap, L.; Bartholomew, D.; Elkind, J.; Melendez, J.; Furlong, C. E. Detection of *Staphylococcus Aureus* Enterotoxin B at Femtomolar Levels with a Miniature Integrated Two-Channel Surface Plasmon Resonance (SPR) Sensor. *Biosens. Bioelectron.* **2002**, *17*, 573–584.
- (23) Zhang, H. Q.; Boussaad, S.; Tao, N. J. High-Performance Differential Surface Plasmon Resonance Sensor Using Quadrant Cell Photodetector. *Rev. Sci. Instrum.* **2003**, *74*, 150–153.
- (24) Hastings, J. T.; Guo, J.; Keathley, P. D.; Kumaresh, P. B.; Wei, Y.; Law, S.; Bachas, L. G. Optimal Self-Referenced Sensing Using Long- and Short- Range Surface Plasmons. *Opt. Express* **2007**, *15*, 17661.
- (25) Zeng, B.; Gao, Y.; Bartoli, F. J. Differentiating Surface and Bulk Interactions in Nanoplasmonic Interferometric Sensor Arrays. *Nano-scale* **2015**, *7*, 166–170.
- (26) Nehru, N.; Donev, E. U.; Huda, G. M.; Yu, L.; Wei, Y.; Hastings, J. T. Differentiating Surface and Bulk Interactions Using Localized Surface Plasmon Resonances of Gold Nanorods. *Opt. Express* **2012**, *20*, 6905.
- (27) Nehru, N.; Yu, L.; Wei, Y.; Hastings, J. T. Using U-Shaped Localized Surface Plasmon Resonance Sensors to Compensate for Nonspecific Interactions. *IEEE Trans. Nanotechnol.* **2014**, *13*, 55–61.
- (28) Neshasteh, H.; Mataji-Kojouri, A.; Akbarzadeh-Jahromi, S. A.; Shahabadi, M. A Hybrid Photonic-Plasmonic Sensing Platform for Differentiating Background and Surface Interactions Using an Array of Metal-Insulator-Metal Resonators. *IEEE Sens. J.* **2016**, *16*, 1621–1627.
- (29) Shahabadi, M.; Schunemann, K. Millimeter-Wave Holographic Power Splitting/Combining. *IEEE Trans. Microwave Theory Tech.* **1997**, *45*, 2316–2323.
- (30) Shahabadi, M.; Atakaramians, S.; Hojjat, N. Transmission Line Formulation for the Full-Wave Analysis of Two-Dimensional Dielectric Photonic Crystals. *IEE Proc.: Sci., Meas. Technol.* **2004**, *151*, 327–334.
- (31) Jason-Moller, L.; Murphy, M.; Bruno, J. Overview of Biacore Systems and Their Applications. *Curr. Protoc. protein Sci.* **2006**, *45*, 13–19.
- (32) Tsortos, A.; Papadakis, G.; Mitsakakis, K.; Melzak, K. A.; Gizeli, E. Quantitative Determination of Size and Shape of Surface-Bound DNA Using an Acoustic Wave Sensor. *Biophys. J.* **2008**, *94*, 2706–2715.
- (33) Rosano, C.; Arosio, P.; Bolognesi, M. The X-Ray Three-Dimensional Structure of Avidin. *Biomol. Eng.* **1999**, *16*, 5–12.
- (34) Cui, J.; Schlub, T. E.; Holmes, E. C. An Allometric Relationship between the Genome Length and Virion Volume of Viruses. *J. Virol.* **2014**, *88*, 6403–6410.
- (35) Liu, F.; Vermesh, O.; Mani, V.; Ge, T. J.; Madsen, S. J.; Sabour, A.; Hsu, E. C.; Gowrishankar, G.; Kanada, M.; Jokerst, J. V.; Sierra, R. G.; Chang, E.; Lau, K.; Sridhar, K.; Bermudez, A.; Pitteri, S. J.; Stoyanova, T.; Sinclair, R.; Nair, V. S.; Gambhir, S. S.; et al. The Exosome Total Isolation Chip. *ACS Nano* **2017**, *11*, 10712–10723.
- (36) Inci, F.; Saylan, Y.; Kojouri, A. M.; Ogut, M. G.; Denizli, A.; Demirci, U. A Disposable Microfluidic-Integrated Hand-Held Plasmonic Platform for Protein Detection. *Appl. Mater. Today* **2020**, *18*, 100478.
- (37) Chia, B. S.; Low, Y. P.; Wang, Q.; Li, P.; Gao, Z. Advances in Exosome Quantification Techniques. *TrAC, Trends Anal. Chem.* **2017**, *86*, 93–106.
- (38) Asghar, W.; Yuksekkaya, M.; Shafiee, H.; Zhang, M.; Ozen, M. O.; Inci, F.; Kocakulak, M.; Demirci, U. Engineering Long Shelf Life Multi-Layer Biologically Active Surfaces on Microfluidic Devices for Point of Care Applications. *Sci. Rep.* **2016**, *6*, 1–10.
- (39) Inci, F.; Ozen, M. O.; Saylan, Y.; Miansari, M.; Cimen, D.; Dhara, R.; Chinnasamy, T.; Yuksekkaya, M.; Filippini, C.; Kumar, D. K.; Calamak, S.; Yesil, Y.; Durmus, N. G.; Duncan, G.; Klevan, L.; Demirci, U. A Novel On-Chip Method for Differential Extraction of Sperm in Forensic Cases. *Adv. Sci.* **2018**, *5*, 1800121.
- (40) Yuan, K.; Shamskhov, E. A.; Orcholski, M. E.; Nathan, A.; Reddy, S.; Honda, H.; Mani, V.; Zeng, Y.; Ozen, M. O.; Wang, L.; Demirci, U.; Tian, W.; Nicolls, M. R.; De Jesus Perez, V. A. Loss of Endothelium-Derived Wnt5a Is Associated with Reduced Pericyte Recruitment and Small Vessel Loss in Pulmonary Arterial Hypertension. *Circulation* **2019**, *139*, 1710–1724.
- (41) Johnson, P. B.; Christy, R. W. Optical Constants of the Noble Metals. *Phys. Rev. B* **1972**, *6*, 4370–4379.